

DeformMaster: An Interactive Physics-Neural World Model for Deformable Objects from Videos

Can Li^{1,*}, Zhoujian Li², Ren Li³, Jie Gu⁴, Lei Lei⁵, Jingmin Chen⁴, Lei Sun¹

¹Nankai University ²Zhejiang University ³Southern University of Science and Technology

⁴Rightly Robotics, A4X ⁵University of Science and Technology of China

Project page: DeformMaster

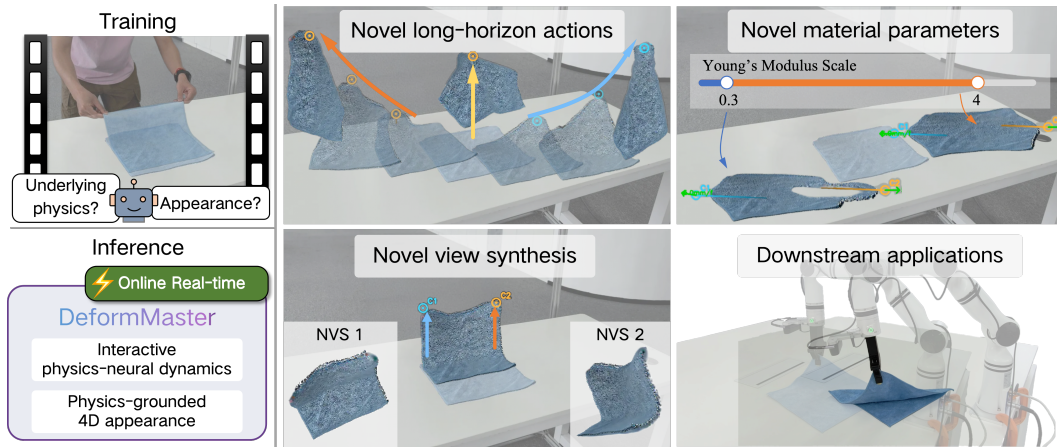


Figure 1: DeformMaster turns a phone-captured monocular video of deformable objects into an online interactive world model. By recovering both underlying physics and high-fidelity appearance, it supports long-horizon rollouts under novel actions, material-parameter variation, and novel-view synthesis, facilitating downstream embodied applications.

Abstract

World models for deformable objects should recover not only geometry and appearance, but also underlying physical dynamics, interaction grounding, and material behavior. Learning such a model from real videos is challenging because deformable linear, planar, and volumetric objects evolve under high-dimensional deformation, noisy interactions, and complex material response. The model must therefore infer a physical state from visual observations, roll it forward under new interactions, and render the resulting dynamics with high visual fidelity. We present DeformMaster, a video-derived interactive physics–neural world model that turns real interaction videos into an online interactive model of deformable objects within a unified dynamics-and-appearance framework. DeformMaster preserves structured physical rollout while using a neural residual to compensate for unmodeled effects, grounds sparse hand motion as distributed compliant actuator for hand–continuum interaction, represents material response with spatially varying constitutive experts, and drives high-fidelity 4D appearance from the predicted physical evolution. Experiments on real-world deformable-object sequences demonstrate DeformMaster’s ability to roll out future dynamics and render dynamic appearance, outperforming state-of-the-art baselines while supporting novel action rollout, material-parameter variation, and dynamic novel-view synthesis.

1 Introduction

World models should encompass not only scene geometry, appearance, and temporal motion, but also the underlying physical attributes, governing dynamics, and causal interactions. Such models are especially important for embodied AI, where an agent must predict how the world will change under its own actions rather than merely reconstructions of observations. Deformable objects make this goal particularly challenging: linear, planar, and volumetric objects evolve in high-dimensional state spaces, and their evolution is dictated by distributed strain, complex material response, self-contact, and external forces. A useful deformable-object world model must therefore infer the underlying physical state, support online interaction by rolling it forward under novel actions, and render its evolving appearance from novel views.

Existing methods have made some progress in reconstructing or generating dynamic deformable scenes. Neural and Gaussian representations can recover high-quality appearance from observations, and physics-aware reconstruction methods further fit physics engines for deformable objects from visual observations [Li et al., 2023, Cai et al., 2024, Zhong et al., 2024, Jiang et al., 2025]. However, parameter identification within an idealized physics model can still struggle to account for real-world phenomena beyond the model assumptions. Recent works further exploit video diffusion either as a dynamic prior to supervise physics fitting [Zhang et al., 2024c, Liu et al., 2025] or as a generative engine for 4D synthesis [Chen et al., 2025, Lu et al., 2026]. However, generative models [Yang et al., 2025] primarily imagine how the world looks; they often lack a reliable understanding of action-conditioned dynamics, making them difficult to control through explicit interactions and prone to hallucinated dynamics that do not match the real physical scene.

Several lines of work attempt to introduce physical controllability, but each leaves a critical gap. Physical digital twins such as PhysTwin [Jiang et al., 2025] and Spring-Gaus [Zhong et al., 2024] couple simulation substrates with Gaussian appearance, while EMPM [Chen et al., 2026] fits differentiable MPM [Hu et al., 2018] for deformable object manipulation; yet fixed physics substrates and pure parameter fitting can hinder the model’s ability to generalize to diverse real-world videos. Learned dynamics models based on particle-graph or particle-grid networks improve flexibility [Sanchez-Gonzalez et al., 2020, Zhang et al., 2025a, 2024b,a]. However, fully learned transitions often suffer from heavy data dependency, remain tied to the training distribution, and drift significantly during long-horizon novel-action rollouts. Hybrid physics-generative systems use physics to carry action semantics into 4D content [Li et al., 2025, Zhan et al., 2026, Liu et al., 2026], but they primarily target generation rather than learning an interactive and physically-realistic model from real observations.

Our key insight is that real-world deformable-object world modeling should jointly recover underlying physical dynamics, interaction grounding, complex material behavior, and appearance tied to the evolving physical state. This requires more than fitting a simulator or learning visual motion alone: the model must remain stable under long-horizon interaction, absorb deviations from idealized physics, translate noisy observed contacts into effective actuation, and keep rendered appearance consistent with the predicted physical evolution. To address these requirements, we propose DeformMaster, an interactive physics–neural world model that turns real interaction videos into an online queryable representation for novel action rollout, novel material-parameter variation, and dynamic novel-view synthesis, as illustrated in Figure 1.

We summarize our core contributions as follows:

1. We propose Physics–Neural Particle–Grid Dynamics (PNPGD) that augments differentiable physics with a neural residual, preserving physics-guided rollouts while compensating for unmodeled real-world effects.
2. We propose Distributed Compliant Actuators (DCA), which turn noisy sparse hand tracks into compliant, spatially distributed actuation for stable and effective hand-continuum interaction.
3. We introduce a Mixture of Constitutive Experts (MoCE) that blends canonical material laws with spatially varying weights to capture heterogeneous material response.
4. We develop DeformMaster, a video-derived deformable-object world model that pairs interactive physics–neural dynamics with physics-grounded high-fidelity 4D appearance.

The rest of the paper is organized as follows. Section 2 reviews related works. Section 3 and Section 4 present our proposed DeformMaster and its evaluation. Section 5 concludes the paper.

2 Related Work

Reconstruction and physics simulation of deformable objects. Physics-based reconstruction methods recover simulatable deformable objects by fitting geometry, appearance, and physical parameters to visual observations. PAC-NeRF [Li et al., 2023], GIC [Cai et al., 2024], PhysGaussian [Xie et al., 2024], OmniPhysGS [Lin et al., 2025], PhysSplat [Zhao et al., 2025], PhysGM [Lv et al., 2026], and NGFF [Li et al., 2026] embed continuum simulation into neural or Gaussian scene representations, while PhysDreamer [Zhang et al., 2024c], PhysFlow [Liu et al., 2025], PhysGen3D [Chen et al., 2025], and Phys4D [Lu et al., 2026] use generative or foundation-model supervision to synthesize plausible 4D dynamics. These works validate physics priors for reconstruction, but generative models [Yang et al., 2025, Zhang et al., 2025c] remain difficult to control through explicit actions, and physical digital twins can be limited by fixed substrates, pure parameter fitting, or brittle action grounding. Closest to our setting, PhysTwin [Jiang et al., 2025, Zhang et al., 2025b] and Spring-Gaus [Zhong et al., 2024] couple physics substrates with Gaussian appearance from RGB-D videos, and EMPM [Chen et al., 2026] fits differentiable MPM for manipulation. We instead use physics–neural dynamics as the core transition model, together with compliant distributed actuation and heterogeneous constitutive modeling, to turn reconstruction into interactive modeling.

Neural dynamics of deformable objects. Learning-based simulators replace analytical dynamics with neural transition models [Ai et al., 2025]. Particle graph [Sanchez-Gonzalez et al., 2020] and particle-grid networks [Zhang et al., 2025a] model ropes, cloths, and volumetric objects; GS-Dynamics [Zhang et al., 2024b] couples Gaussian tracking with graph dynamics, and AdaptiGraph [Zhang et al., 2024a] conditions graph dynamics on physical-property estimates. These methods are flexible, but purely learned transitions often need substantial data, remain tied to the training distribution, and drift under long rollouts or novel actions. We instead use a physics-guided rollout for stronger generalization, with neural dynamics acting as a residual correction for real-world mismatch.

Hybrid physics-generative world models. Recent systems also use physics to support action-conditioned 4D world prediction. Building on the static-scene precursor WonderWorld [Yu et al., 2025], the Wonder series couples physics solvers with video generation for interactive content creation through WonderPlay [Li et al., 2025], PerpetualWonder [Zhan et al., 2026], and RealWonder [Liu et al., 2026]. Force Prompting [Gillman et al., 2025] and Goal Force [Gillman et al., 2026] further fine-tune video diffusion models on synthetic physics primitives to absorb force control signals. These methods show that physics can guide video generation, but require large-scale generative-model training. We instead learn from real videos the underlying physics in a data-efficient way.

3 DeformMaster

We seek a world model of deformable objects that (i) rolls out stable dynamics aligned with real-world observations, (ii) grounds noisy hand tracks for effective hand–continuum interaction, (iii) captures complex material response, and (iv) renders high-fidelity appearance grounded in physics. To this end, as illustrated in Figure 2, DeformMaster pairs interactive physics–neural dynamics (Section 3.2) with physics-grounded appearance (Section 3.3) through four components: PNP GD for dynamics rollout, DCA for interaction, MoCE for material response, and Gaussian Splatting for rendering.

3.1 Problem Formulation

State. We represent the deformable state as $s_t = (s_t^{\text{mat}}, s_t^{\text{app}})$, where s_t^{mat} denotes the material-particle state and s_t^{app} the appearance-particle state. **Actions.** The action a_t consists of observed hand or actuator anchor positions and velocities. **Observations.** Supervision comes from monocular or multi-view RGB-D videos with extracted point clouds, camera poses, and dense 3D tracks. **Learning objective.** We learn (θ, ϕ, ψ) for the joint dynamics-appearance model:

$$s_{t+1}^{\text{mat}} = \mathcal{F}_{\theta, \phi}(s_t^{\text{mat}}, a_t), \quad \hat{I}_{t+1} = \mathcal{G}_{\psi}(s_{t+1}^{\text{app}}) = \mathcal{G}_{\psi}(\mathcal{B}_{\psi}(s_{t+1}^{\text{mat}})), \quad (1)$$

where $\mathcal{F}_{\theta, \phi}$ is the hybrid physics–neural rollout operator for material dynamics; \mathcal{B}_{ψ} bridges material particles to appearance particles; and \mathcal{G}_{ψ} renders that state into images. Training matches both rolled-out material states and rendered frames to observations.

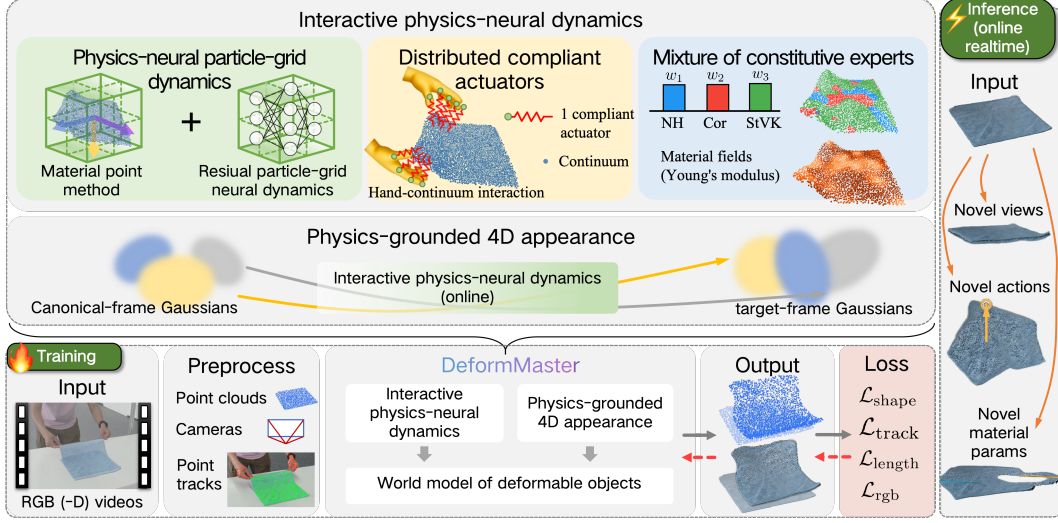


Figure 2: Overview of DeformMaster. From interaction videos, DeformMaster unifies interactive physics–neural dynamics and physics-grounded 4D appearance in a single deformable-object world model. The dynamics module integrates Physics–Neural Particle–Grid Dynamics, Distributed Compliant Actuators, and a Mixture of Constitutive Experts to support stable rollout, robust hand–continuum interaction, and heterogeneous material response. Gaussian splats are driven by the dynamics branch. Inference supports novel view, action, and material-parameter conditions online.

3.2 Interactive Physics–Neural Dynamics

Physics–Neural Particle–Grid Dynamics (PNPGD). Physics-based simulators provide structured, stable priors for dynamics, but real observations exhibit systematic effects that no idealized model can fully express. We therefore pair an explicit physics block with a neural residual that absorbs the unmodeled mismatch.

We decompose deformation dynamics $\mathcal{F}_{\theta, \phi}$ into a physics block \mathcal{P}_{θ} and a residual block \mathcal{R}_{ϕ} :

$$\mathcal{F}_{\theta, \phi} = \mathcal{P}_{\theta} \oplus \mathcal{R}_{\phi}. \quad (2)$$

Concretely, \mathcal{P}_{θ} first advances the state over one frame with differentiable MPM [Hu et al., 2018] under material parameters θ , producing a tentative next state (with s_t denoting s_t^{mat} for brevity):

$$\tilde{s}_{t+1} = \mathcal{P}_{\theta}^{\text{MPM}}(s_t, a_t), \quad (3)$$

where $s_t = (\mathbf{x}_p^t, \mathbf{v}_p^t, \mathbf{F}_p^t, \mathbf{C}_p^t)$ is the MPM particle state consisting of per-particle position, velocity, deformation gradient, and affine matrix; a_t denotes the action (detailed in DCA below). Second, after the MPM rollout over one frame, a residual block \mathcal{R}_{ϕ} predicts a neural velocity correction $\Delta \mathbf{v}_p$,

$$\Delta \mathbf{v}_p = \mathcal{R}_{\phi}(\tilde{s}_{t+1}, s_t, h_t), \quad (4)$$

where $h_t = \{(\mathbf{x}_p^{t-i}, \mathbf{v}_p^{t-i})\}_{i=1}^H$ is a short kinematic history. The final residual-corrected state s_{t+1} is then given by

$$\mathbf{v}_p^{t+1} = \tilde{\mathbf{v}}_p^{t+1} + \Delta \mathbf{v}_p, \quad \mathbf{x}_p^{t+1} = \tilde{\mathbf{x}}_p^{t+1} + \Delta \mathbf{v}_p \Delta t, \quad (5)$$

where the residual updates only particle positions and velocities, while \mathbf{F}_p^{t+1} and \mathbf{C}_p^{t+1} are inherited from \tilde{s}_{t+1} . By design $\|\Delta \mathbf{v}_p\|$ is bounded, so \mathcal{R}_{ϕ} acts as a perturbation at the frame level rather than a free state predictor.

To compose cleanly with MPM, residual block \mathcal{R}_{ϕ} uses a similar particle-grid representation. We reformulate Particle-Grid Neural Dynamics [Zhang et al., 2025a] as this residual block: a PointNet encoder [Qi et al., 2017] produces a per-particle latent feature

$$\mathbf{f}_p = E_{\phi}(\tilde{\mathbf{x}}_p^{t+1}, \tilde{\mathbf{v}}_p^{t+1}, \tilde{\mathbf{x}}_p^{t+1} - \mathbf{x}_p^t, h_t), \quad (6)$$

that summarises the post-MPM state and history h_t ; a coordinate-conditioned MLP decoder with Fourier positional encoding [Mildenhall et al., 2020] predicts a bounded grid-node correction $\mathbf{u}_g =$

$\alpha \tanh(\cdot)$, which is then mapped back to particles by the same B-spline weights MPM uses for P2G/G2P transfers, yielding $\Delta \mathbf{v}_p$. The residual architecture mirrors MPM’s particle-grid hybrid through an Eulerian grid representation and particle-grid transfer. Details of the MPM configuration and neural residual architecture are provided in Sections A.3 and A.4.

Distributed Compliant Actuator (DCA). Hand–continuum interaction is often the fragile part of real-to-sim deformable modeling. Vision-derived hand or actuator tracks are noisy and sparse, so hard pointwise constraints surface two failure modes: tracking noise is injected as velocity spikes, and point loads deform only a tiny neighborhood. DCA addresses these failure modes with *compliance*, which turns hard constraints into compliant actuator-particle couplings absorbing high-frequency noise, and *distribution*, which spreads actuation over a finite contact patch to drive bulk motion in a soft continuum.

Concretely, DCA applies compliant actuator-to-particle couplings over a local actuator neighborhood, producing the actuator-induced acceleration \mathbf{a}_p on particle p :

$$\mathbf{a}_p = n_p^{-1/2} \sum_{c \in \mathcal{N}(p)} \left[k_p ((\mathbf{x}_c - \mathbf{x}_p) - \mathbf{o}_{p,c}^0) + k_d (\mathbf{v}_c - \mathbf{v}_p) \right], \quad (7)$$

where k_p, k_d are stiffness and damping (DCA gains), $\mathbf{x}_p, \mathbf{v}_p$ are the particle state, $\mathbf{x}_c, \mathbf{v}_c$ are actuator-anchor state, $\mathbf{o}_{p,c}^0$ is the initial rest offset, $\mathcal{N}(p)$ is the local actuator neighborhood, $n_p = |\mathcal{N}(p)|$. The $n_p^{-1/2}$ factor normalizes over multiple anchors to avoid force stacking.

Mixture of Constitutive Experts (MoCE). Real deformable objects rarely conform to a single idealized constitutive law. Their response is shaped by material composition, processing history, and scene-specific deformation patterns. We therefore represent stress with a finite mixture of constitutive experts whose weights can adapt across continuum regions. We model the first Piola–Kirchhoff stress as a spatially varying mixture of constitutive experts:

$$\mathbf{P}_{\text{mix}}(\mathbf{F}_p; E_p, \nu_p) = \sum_k w_{k,p} \mathbf{P}_k(\mathbf{F}_p; E_p, \nu_p), \quad (8)$$

where \mathbf{P}_k is the stress map of expert $k \in \{\text{NH}, \text{Cor}, \text{StVK}\}$, \mathbf{F}_p is the deformation gradient of particle p , and E_p, ν_p denote learnable Young’s modulus and Poisson’s ratio. The mixture weights $w_{k,p}$ are spatially varying, implemented through patch-level expert logits and interpolated to particles as detailed in Section A.5.

3.3 Physics-Grounded 4D Appearance

Online interaction requires high-fidelity rendering without re-optimizing a dynamic appearance model after every new action. We therefore keep rollout on a compact material-particle state and use it to drive Gaussian appearance. Given the particle trajectory predicted by $\mathcal{F}_{\theta, \phi}$, the bridge \mathcal{B}_ψ deforms Gaussians using LBS [Sumner et al., 2007, Huang et al., 2024]. The update is incremental: each frame applies the particle motion from the previous frame to the current one, rather than re-skinning from the canonical state. This keeps rendering efficient and aligned with physical motion without learning a separate dynamic reconstruction model.

3.4 Training Scheme

We train DeformMaster with a combined dynamics-and-appearance objective:

$$\mathcal{L}_{\text{total}} = \mathcal{L}_{\text{dynamics}} + \mathcal{L}_{\text{appearance}} = \lambda_{\text{track}} \mathcal{L}_{\text{track}} + \lambda_{\text{shape}} \mathcal{L}_{\text{shape}} + \lambda_{\text{len}} \mathcal{L}_{\text{len}} + \lambda_{\text{rgb}} \mathcal{L}_{\text{rgb}}, \quad (9)$$

where $\mathcal{L}_{\text{dynamics}}$ contains track, shape, and length terms: $\mathcal{L}_{\text{track}}$ aligns 3D point trajectories, $\mathcal{L}_{\text{shape}}$ aligns shape with Chamfer distance, and \mathcal{L}_{len} preserves local lengths. $\mathcal{L}_{\text{appearance}}$ is \mathcal{L}_{rgb} , a photometric loss on rendered frames. Optimization proceeds in multiple stages. Stages 1–2 alternate between dynamics training and DCA gain selection: we first learn the material fields and neural residual with default DCA gains under dynamics loss, use the warm-started dynamics to select gains with CMA-ES [Hansen, 2006], and then continue learning the material fields and neural residual with the updated gains. Stage 3 first optimizes Gaussian splats with appearance loss and then uses the total loss (*i.e.*, adding RGB loss) to refine the dynamics branch.

Table 1: Overall future-prediction comparison on 20 real-world PhysTwin deformation sequences. We report dynamics accuracy and rendered appearance quality averaged over unseen test frames. DeformMaster achieves the strongest overall performance, improving dynamics and appearance fidelity while remaining comparable to PhysTwin on Track error.

Method	Future dynamics			Future appearance		
	IoU \uparrow	Chamfer \downarrow	Track \downarrow	PSNR \uparrow	SSIM \uparrow	LPIPS \downarrow
PhysTwin [Jiang et al., 2025]	0.734	0.012	0.023	25.16	0.935	0.061
Spring-Gaus [Zhong et al., 2024]	0.464	0.062	0.094	22.49	0.924	0.113
GS-Dynamics [Zhang et al., 2024b]	0.498	0.041	0.070	22.54	0.924	0.097
DeformMaster (ours)	0.748	0.011	0.024	25.41	0.936	0.061

Table 2: Per-category dynamics prediction on the PhysTwin sequences, grouped into deformable linear, planar, and volumetric objects. DeformMaster improves on linear and volumetric objects, while the remaining Track gap is concentrated in planar object sequences.

Method	Linear ($n=3$)			Planar ($n=9$)			Volumetric ($n=8$)		
	IoU \uparrow	Chamfer \downarrow	Track \downarrow	IoU \uparrow	Chamfer \downarrow	Track \downarrow	IoU \uparrow	Chamfer \downarrow	Track \downarrow
PhysTwin [Jiang et al., 2025]	0.658	0.007	0.013	0.738	0.013	0.028	0.748	0.013	0.021
DeformMaster (ours)	0.721	0.005	0.010	0.748	0.013	0.032	0.756	0.012	0.020

4 Experiments

4.1 Setup

We organize the evaluation around the contributions of DeformMaster. **Implementation.** Implementation details (preprocessing, MPM, neural residual, MoCE, and training) are deferred to Section A. **Dataset.** We evaluate on 20 real deformable-object sequences from PhysTwin [Jiang et al., 2025], spanning deformable linear ($n=3$, ropes), planar ($n=9$, cloths and package), and volumetric ($n=8$, softbodied toys) objects, all captured with calibrated three-view RGB-D videos at 30 fps. **Baselines.** We compare the full system against PhysTwin [Jiang et al., 2025], Spring-Gaus [Zhong et al., 2024], and GS-Dynamics [Zhang et al., 2024b], and ablate PNP GD, DCA, MoCE, and RGB-guided dynamics refinement (Sections 4.2 and 4.3). **Metrics.** We evaluate future rollout with dynamics metrics (Chamfer distance, Track error, and mask IoU) and appearance metrics (PSNR, SSIM, and LPIPS). **Online playground.** Our method supports online interactive rollout at over 15 fps; the online playground is shown in Section A.1, with additional interactive results on our project page. We will release the code and data for the online interaction upon publication.

4.2 Main Results

Table 1 reports future-frame prediction results on the 20 PhysTwin sequences. Our DeformMaster achieves the strongest overall performance, improving mask IoU and Chamfer distance over all baselines and producing the best rendered appearance. Compared with PhysTwin, our method slightly improves Chamfer (0.011 vs. 0.012) and IoU (0.748 vs. 0.734), while maintaining a comparable Track error (0.024 vs. 0.023). The advantage over learning-based Gaussian dynamics baselines is more pronounced: our method reduces Chamfer by more than $3\times$ and Track error by at least $2.9\times$ compared with Spring-Gaus and GS-Dynamics. Since the appearance metrics are computed by deforming the same first-frame Gaussian representation with the predicted trajectory, the improvements in PSNR, SSIM, and LPIPS mainly reflect better long-horizon rollout rather than renderer-specific tuning.

Table 2 further breaks down the dynamics results by object type. The gains are most pronounced on linear objects (ropes), where our DeformMaster improves IoU from 0.658 to 0.721 and reduces Chamfer and Track error from 0.007/0.013 to 0.005/0.010. On volumetric objects (soft-bodied toys), our method also improves all three dynamics metrics, indicating that the particle-grid-based transition model benefits objects with substantial three-dimensional deformation. Planar objects are the most challenging case: our method slightly improves IoU and matches Chamfer, but its Track error is higher than PhysTwin (0.032 vs. 0.028). This suggests that the small overall Track gap in

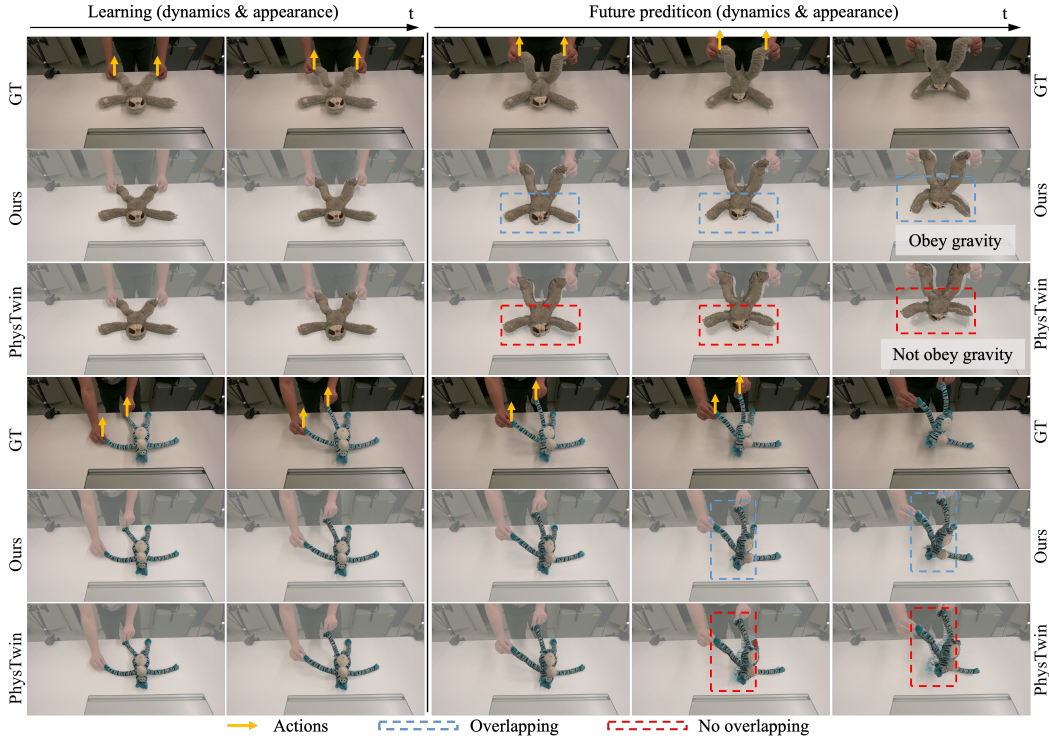


Figure 3: Qualitative comparison on two representative deformation sequences. Columns progress from the learning stage to future prediction, and each case compares ground truth (GT), DeformMaster (Ours), and PhysTwin. Yellow arrows indicate the applied actions. Blue and red dashed boxes mark corresponding regions in our prediction and PhysTwin, respectively. DeformMaster better preserves the future object configuration and yields stronger overlap with GT in the highlighted regions.

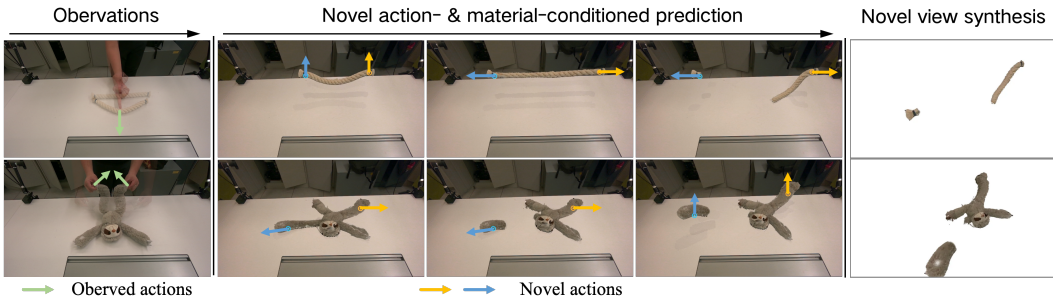


Figure 4: Generalization to novel action-, material-, and view-conditioned prediction with our DeformMaster. DeformMaster supports rollouts under novel actions and material scales. Scaling the material fields to $0.3\times$ their learned values produces fracture behavior, while the final column renders the fracture states from a novel view, demonstrating interactive ability beyond the observations and baselines.

Table 1 is mainly driven by planar sequences, where single-layer cloth-like motion is less naturally matched to the particle-grid continuum simulator.

Figure 3 visualizes two representative deformable volumetric objects from the PhysTwin sequences. During the learning stage, both methods capture the dynamics and appearance well. In future prediction, our method better preserves the object configuration under upward pulling and gravity, and remains more closely aligned with the ground truth in the highlighted regions. These results qualitatively echo the design goals: stable long-horizon rollouts, compensation for idealized-physics mismatch, effective actuation from noisy contacts, and appearance tied to the predicted physical

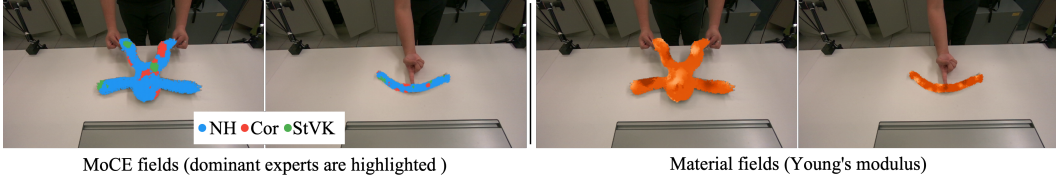


Figure 5: Qualitative visualization of MoCE and material fields. For readability, the left two panels visualize the MoCE mixture by showing only the largest-weight constitutive expert at each particle. The right two panels visualize the material field as the spatial distribution of Young’s modulus. The results qualitatively show that our method captures spatially varying material behavior for deformable objects, rather than assuming a single homogeneous constitutive response.

state. In contrast, PhysTwin tends to under-deform or drift away from the observed shape, leading to weaker overlap in the same regions.

Figure 4 shows that our model can be queried under novel action, material parameters, and view conditions. Starting from the same observed object, our method performs rollouts under novel conditions by changing the actuation direction and material parameter scale, and then renders the predicted state from a novel camera view. Notably, scaling the material fields to $0.3\times$ their recovered values produces material fracture, illustrating a discontinuous behavior that is difficult for PhysTwin’s fixed topological connectivity to express.

Figure 5 visualizes MoCE and material fields on representative deformable objects. In MoCE, each particle uses a mixture over constitutive experts; for readability, the visualization shows only the dominant expert with the largest mixture weight at each particle. The displayed expert maps and the corresponding Young’s modulus fields are spatially non-uniform, indicating that the optimized material response adapts across object regions. Together, these visualizations show that our model captures region-dependent material behavior from video observations, rather than reducing each deformable object to a single homogeneous constitutive response.

4.3 Ablation Study

PNPGD: Residual Matters, and Its Architecture Matters. Figure 6(a) ablates PNPGD by varying the residual branch. We compare the proposed particle-grid residual with three alternatives: removing the residual entirely, using an MLP residual that predicts independent per-particle corrections, and using a GNN residual in the style of particle-based neural simulators [Sanchez-Gonzalez et al., 2020]. The MPM-only variant without residual degrades both dynamics and appearance, confirming that the pure physics simulator provides a useful prior but cannot by itself absorb the systematic mismatch present in real videos. Among residual variants, both the MLP and GNN underperform the proposed design, showing that the particle-grid residual architecture is more effective. Together, these results support the motivation in Section 3.2: a neural residual is needed to bridge the gap between idealized physics and real-world observations, and the particle-grid residual architecture matters. Full numbers are reported in Tables 5 and 6.

DCA: Both Compliance and Distribution Matter. Figure 6(b) ablates the two design choices in DCA. The rigid variant removes compliance by replacing compliant actuator-particle coupling with hard constraints, while the single-actuator variant keeps compliance but collapses each distributed actuator to one actuator. The rigid variant diverges on 9/20 sequences, including all 8 volumetric cases, which is consistent with the motivation that noisy vision-derived tracks should not be injected as hard pointwise constraints. The single-actuator variant is numerically stable but reduces accuracy, showing that pointwise forcing is insufficient to drive bulk deformation in a soft continuum. These results verify the two-part DCA design in Section 3.2: compliance stabilizes action grounding under noisy tracks, and distribution improves force transmission over contact regions of deformable objects. Full numbers are reported in Tables 7 and 8.

MoCE vs. Single Expert. Figure 6(c) ablates the constitutive model by replacing MoCE with a single Neo-Hookean expert while keeping the rest of the pipeline unchanged. This removes the spatially varying constitutive experts and forces all particles to share the same canonical constitutive

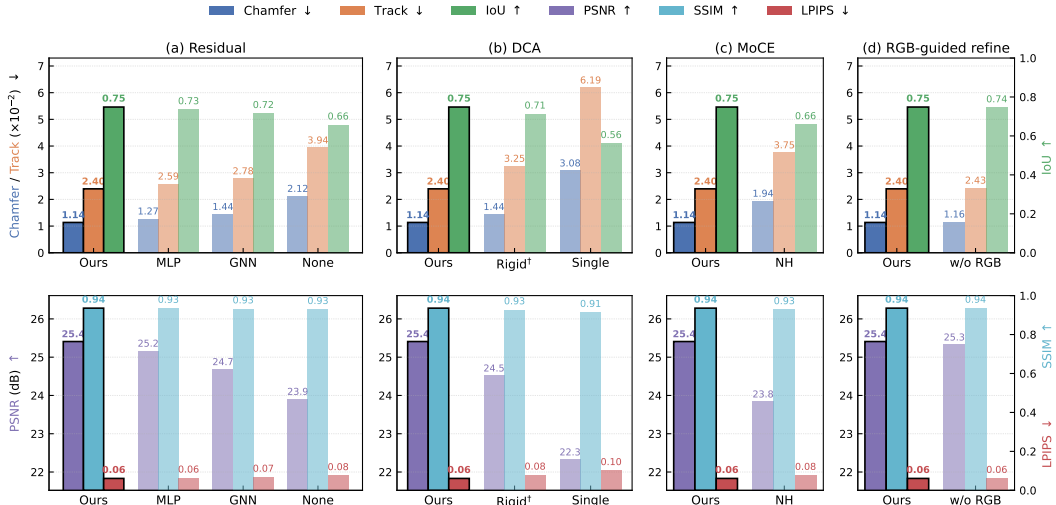


Figure 6: Ablation summary. Columns (a)–(d) compare four design choices, with dynamics metrics in the top row (Chamfer/Track in 10^{-2} , IoU) and appearance metrics in the bottom row (PSNR, SSIM, LPIPS). **(a) Residual**: the neural particle-grid residual performs best, while MLP/GNN residuals and removing the residual (None, *i.e.*, MPM only) degrade both dynamics rollout and appearance. **(b) DCA**: removing compliance (Rigid[†], reported on 11/20 successfully trained sequences) or collapsing the distributed actuator to a single one (Single) both reduce performance, showing the need for distributed compliant actuation. **(c) MoCE**: replacing the mixture with a single Neo-Hookean expert worsens both dynamics and appearance. **(d) RGB-guided refinement**: fine-tuning with RGB loss in training stage 3 improves dynamics metrics and rendered appearance over the dynamics-loss-only variant (w/o RGB). Overall, each component contributes to the final system; “Ours” is highlighted with a solid edge, and full numerical results are in Section A.9.

law. The single-expert variant worsens both rollout accuracy and rendered appearance, indicating that real deformation sequences contain heterogeneous material responses that cannot be fully represented by a global constitutive choice. In contrast, MoCE represents the stress response as a spatially varying mixture of canonical constitutive experts, allowing the model to adapt across continuum regions while remaining grounded in analytic constitutive laws. Full numbers are reported in Tables 9 and 10.

Effect of RGB-Guided Refinement. Figure 6(d) evaluates RGB-guided dynamics refinement by ablating the RGB loss in training stage 3. We compare whether to use the total loss (*i.e.*, adding RGB loss) to refine the dynamics branch. Because the rendered appearance is driven by the predicted material-particle trajectory (Equation (1)), the RGB loss provides supervision to the underlying dynamics rather than only to image-space appearance. Adding this loss yields consistent overall gains, improving both dynamics and rendered appearance metrics. Per-category results in Table 12 show that the dynamics gains mainly come from deformable planar and volumetric objects, while linear objects remain nearly unchanged. These results show that RGB supervision in stage 3 contributes to rollout refinement. Full numbers are reported in Tables 11 and 12.

5 Conclusion

We proposed DeformMaster, a video-derived interactive physics-neural world model for deformable objects. From real interaction videos, DeformMaster couples interactive physics-neural dynamics with physics-grounded appearance, enabling controllable rollout and high-fidelity rendering. This design reflects the central contributions of the paper: robust physics–neural dynamics, stable grounding of real interactions, heterogeneous material modeling, and 4D appearance synthesis driven by the underlying physics. Experiments on multi-category real sequences show the strongest overall future dynamics and appearance, with clear gains over baselines. Ablations further confirm that each component contributes to rollout accuracy and appearance quality. Looking ahead, extending DeformMaster to richer contact, fluid, and robotic manipulation remains a promising direction.

References

- Bo Ai, Stephen Tian, Haochen Shi, Yixuan Wang, Tobias Pfaff, Cheston Tan, Henrik I. Christensen, Hao Su, Jiajun Wu, and Yunzhu Li. A review of learning-based dynamics models for robotic manipulation. *Science Robotics*, 10(106), 2025. doi: 10.1126/scirobotics.adt1497.
- Junhao Cai, Yuji Yang, Weihao Yuan, Yisheng He, Zilong Dong, Liefeng Bo, Hui Cheng, and Qifeng Chen. GIC: Gaussian-informed continuum for physical property identification and simulation. In *Advances in Neural Information Processing Systems (NeurIPS)*, 2024. URL <https://arxiv.org/abs/2406.14927>.
- Boyuan Chen, Hanxiao Jiang, Shaowei Liu, Saurabh Gupta, Yunzhu Li, Hao Zhao, and Shenlong Wang. PhysGen3D: Crafting a miniature interactive world from a single image. In *Proceedings of the IEEE/CVF Conference on Computer Vision and Pattern Recognition (CVPR)*, 2025. URL <https://arxiv.org/abs/2503.20746>.
- Yunuo Chen, Yafei Hu, Lingfeng Sun, Tushar Kusnur, Laura Herlant, and Chenfanfu Jiang. EMPM: Embodied MPM for modeling and simulation of deformable objects. *IEEE Robotics and Automation Letters*, 11(3):4179–4186, 2026. URL <https://arxiv.org/abs/2601.17251>.
- Nate Gillman, Michael Freeman, Daksh Aggarwal, Chia-Hong Hsu, Calvin Luo, Yonglong Tian, and Chen Sun. Force prompting: Video generation models can learn and generalize physics-based control signals. In *Advances in Neural Information Processing Systems (NeurIPS)*, 2025. URL <https://arxiv.org/abs/2505.19386>.
- Nate Gillman, Yinghua Zhou, Zitian Tang, Evan Luo, Arjan Chakravarthy, Daksh Aggarwal, Michael Freeman, Charles Herrmann, and Chen Sun. Goal force: Teaching video models to accomplish physics-conditioned goals. *arXiv preprint arXiv:2601.05848*, 2026. URL <https://arxiv.org/abs/2601.05848>.
- Nikolaus Hansen. The CMA evolution strategy: A comparing review. In Jose A. Lozano, Pedro Larrañaga, Iñaki Inza, and Endika Bengoetxea, editors, *Towards a New Evolutionary Computation: Advances on Estimation of Distribution Algorithms*, volume 192 of *Studies in Fuzziness and Soft Computing*, pages 75–102. Springer, Berlin, Heidelberg, 2006. doi: 10.1007/3-540-32494-1_4.
- Yuanming Hu, Yu Fang, Ziheng Ge, Ziyin Qu, Yixin Zhu, Andre Pradhana, and Chenfanfu Jiang. A moving least squares material point method with displacement discontinuity and two-way rigid body coupling. *ACM Transactions on Graphics*, 37(4), 2018. doi: 10.1145/3197517.3201293.
- Yi-Hua Huang, Yang-Tian Sun, Ziyi Yang, Xiaoyang Lyu, Yan-Pei Cao, and Xiaojuan Qi. SC-GS: Sparse-controlled gaussian splatting for editable dynamic scenes. In *Proceedings of the IEEE/CVF Conference on Computer Vision and Pattern Recognition (CVPR)*, 2024. URL <https://arxiv.org/abs/2312.14937>.
- Hanxiao Jiang, Hao-Yu Hsu, Kaifeng Zhang, Hsin-Ni Yu, Shenlong Wang, and Yunzhu Li. PhysTwin: Physics-informed reconstruction and simulation of deformable objects from videos. In *Proceedings of the IEEE/CVF International Conference on Computer Vision (ICCV)*, 2025. URL <https://arxiv.org/abs/2503.17973>.
- Nikita Karaev, Iurii Makarov, Jianyuan Wang, Natalia Neverova, Andrea Vedaldi, and Christian Rupprecht. CoTracker3: Simpler and better point tracking by pseudo-labelling real videos. *arXiv preprint arXiv:2410.11831*, 2024. URL <https://arxiv.org/abs/2410.11831>.
- Shiqian Li, Ruihong Shen, Junfeng Ni, Chang Pan, Chi Zhang, and Yixin Zhu. Learning physics-grounded 4D dynamics with neural gaussian force fields. In *International Conference on Learning Representations (ICLR)*, 2026. URL <https://arxiv.org/abs/2602.00148>.
- Xuan Li, Yi-Ling Qiao, Peter Yichen Chen, Krishna Murthy Jatavallabhula, Ming Lin, Chenfanfu Jiang, and Chuang Gan. PAC-NeRF: Physics augmented continuum neural radiance fields for geometry-agnostic system identification. In *International Conference on Learning Representations (ICLR)*, 2023. URL <https://arxiv.org/abs/2303.05512>.

- Zizhang Li, Hong-Xing Yu, Wei Liu, Yin Yang, Charles Herrmann, Gordon Wetzstein, and Jiajun Wu. WonderPlay: Dynamic 3D scene generation from a single image and actions. In *Proceedings of the IEEE/CVF International Conference on Computer Vision (ICCV)*, 2025. URL <https://arxiv.org/abs/2505.18151>.
- Haotong Lin, Sili Wang, Jingxiao Wu, Lujia Yang, Hengshuang Wang, Tao Wang, Tianqi Yang, Junfei Wang, Tianhe Bai, Heng Yu, Hengshuang Zhao, and Bingyi Yang. Depth anything 3: Recovering the visual space from any views. In *International Conference on Learning Representations (ICLR)*, 2026. URL <https://arxiv.org/abs/2511.10647>.
- Yuchen Lin, Chenguo Lin, Jianjin Xu, and Yadong Mu. OmniPhysGS: 3D constitutive gaussians for general physics-based dynamics generation. In *International Conference on Learning Representations (ICLR)*, 2025. URL <https://arxiv.org/abs/2501.18982>.
- Wei Liu, Ziyu Chen, Zizhang Li, Yue Wang, Hong-Xing Yu, and Jiajun Wu. RealWonder: Real-time physical action-conditioned video generation. *arXiv preprint arXiv:2603.05449*, 2026. URL <https://arxiv.org/abs/2603.05449>.
- Zhuoman Liu, Weicai Ye, Yan Luximon, Pengfei Wan, and Di Zhang. PhysFlow: Unleashing the potential of multi-modal foundation models and video diffusion for 4D dynamic physical scene simulation. In *Proceedings of the IEEE/CVF Conference on Computer Vision and Pattern Recognition (CVPR)*, 2025. URL <https://arxiv.org/abs/2411.14423>.
- Haoran Lu, Shang Wu, Jianshu Zhang, Maojiang Su, Guo Ye, Chenwei Xu, Lie Lu, Pranav Maneriker, Fan Du, Manling Li, Zhaoran Wang, and Han Liu. Phys4D: Fine-grained physics-consistent 4D modeling from video diffusion. *arXiv preprint arXiv:2603.03485*, 2026. URL <https://arxiv.org/abs/2603.03485>.
- Chunji Lv, Zequn Chen, Donglin Di, Weinan Zhang, Hao Li, Wei Chen, Yinjie Lei, and Changsheng Li. PhysGM: Large physical gaussian model for feed-forward 4D synthesis. In *Proceedings of the IEEE/CVF Conference on Computer Vision and Pattern Recognition (CVPR)*, 2026. URL <https://arxiv.org/abs/2508.13911>.
- Ben Mildenhall, Pratul P. Srinivasan, Matthew Tancik, Jonathan T. Barron, Ravi Ramamoorthi, and Ren Ng. NeRF: Representing scenes as neural radiance fields for view synthesis. In *European Conference on Computer Vision (ECCV)*, 2020.
- Charles R. Qi, Hao Su, Kaichun Mo, and Leonidas J. Guibas. PointNet: Deep learning on point sets for 3D classification and segmentation. In *Proceedings of the IEEE Conference on Computer Vision and Pattern Recognition (CVPR)*, 2017.
- Tianhe Ren, Shilong Liu, Qing Jiang, Yihao Wei, Zhaoyang Zeng, Jing Yang, Wenlong Liu, Hao Wang, Feng Liang, Hao Zhang, Lei Yang, and Lei Zhang. Grounded SAM 2: Ground and track anything in videos with grounding DINO, Florence-2 and SAM 2. <https://github.com/IDEA-Research/Grounded-SAM-2>, 2024. IDEA Research open-source implementation.
- Alvaro Sanchez-Gonzalez, Jonathan Godwin, Tobias Pfaff, Rex Ying, Jure Leskovec, and Peter W. Battaglia. Learning to simulate complex physics with graph networks. In *Proceedings of the 37th International Conference on Machine Learning (ICML)*, 2020. URL <https://arxiv.org/abs/2002.09405>.
- Paul-Edouard Sarlin, Daniel DeTone, Tomasz Malisiewicz, and Andrew Rabinovich. SuperGlue: Learning feature matching with graph neural networks. In *Proceedings of the IEEE/CVF Conference on Computer Vision and Pattern Recognition (CVPR)*, 2020. URL <https://arxiv.org/abs/1911.11763>.
- Robert W. Sumner, Johannes Schmid, and Mark Pauly. Embedded deformation for shape manipulation. *ACM Transactions on Graphics*, 26(3), 2007. doi: 10.1145/1275808.1276478.
- Ruicheng Wang, Sicheng Xu, Cassie Yang, Yue Yuan, Xin Tong, and Jiaolong Yang. MoGe-2: Accurate monocular geometry with metric scale and sharp details. In *Advances in Neural Information Processing Systems (NeurIPS)*, 2025. URL <https://arxiv.org/abs/2507.02546>.

- Jianfeng Xiang, Zelong Lv, Sicheng Xu, Yu Deng, Ruicheng Wang, Bowen Zhang, Dong Chen, Xin Tong, and Jiaolong Yang. Structured 3D latents for scalable and versatile 3D generation. In *Proceedings of the IEEE/CVF Conference on Computer Vision and Pattern Recognition (CVPR)*, 2025. URL <https://arxiv.org/abs/2412.01506>.
- Tianyi Xie, Zeshun Zong, Yuxing Qiu, Xuan Li, Yutao Feng, Yin Yang, and Chenfanfu Jiang. PhysGaussian: Physics-integrated 3D gaussians for generative dynamics. In *Proceedings of the IEEE/CVF Conference on Computer Vision and Pattern Recognition (CVPR)*, 2024. URL <https://arxiv.org/abs/2311.12198>.
- Zhuoyi Yang, Jiayan Teng, Wendi Zheng, Ming Ding, Shiyu Huang, Jiazheng Xu, Yuanming Yang, Wenyi Hong, Xiaohan Zhang, Guanyu Feng, Da Yin, Xiaotao Gu, Yuxuan Zhang, Weihang Wang, Yean Cheng, Ting Liu, Bin Xu, Yuxiao Dong, and Jie Tang. CogVideoX: Text-to-video diffusion models with an expert transformer. In *International Conference on Learning Representations (ICLR)*, 2025. URL <https://arxiv.org/abs/2408.06072>.
- Hong-Xing Yu, Haoyi Duan, Charles Herrmann, William T. Freeman, and Jiajun Wu. WonderWorld: Interactive 3D scene generation from a single image. In *Proceedings of the IEEE/CVF Conference on Computer Vision and Pattern Recognition (CVPR)*, 2025. URL <https://arxiv.org/abs/2406.09394>.
- Jiahao Zhan, Zizhang Li, Hong-Xing Yu, and Jiajun Wu. PerpetualWonder: Long-horizon action-conditioned 4D scene generation. *arXiv preprint arXiv:2602.04876*, 2026. URL <https://arxiv.org/abs/2602.04876>.
- Kaifeng Zhang, Baoyu Li, Kris Hauser, and Yunzhu Li. AdaptiGraph: Material-adaptive graph-based neural dynamics for robotic manipulation. In *Proceedings of Robotics: Science and Systems (RSS)*, 2024a. URL <https://arxiv.org/abs/2407.07889>.
- Kaifeng Zhang, Baoyu Li, Kris Hauser, and Yunzhu Li. Particle-grid neural dynamics for learning deformable object models from RGB-D videos. In *Proceedings of Robotics: Science and Systems (RSS)*, 2025a. URL <https://arxiv.org/abs/2506.15680>.
- Kaifeng Zhang, Shuo Sha, Hanxiao Jiang, Matthew Loper, Hyunjong Song, Guangyan Cai, Zhuo Xu, Xiaochen Hu, Changxi Zheng, and Yunzhu Li. Real-to-sim robot policy evaluation with Gaussian splatting simulation of soft-body interactions. *arXiv preprint arXiv:2511.04665*, 2025b. URL <https://arxiv.org/abs/2511.04665>.
- Mingtong Zhang, Kaifeng Zhang, and Yunzhu Li. Dynamic 3D gaussian tracking for graph-based neural dynamics modeling. In *Proceedings of the 8th Conference on Robot Learning (CoRL)*, 2024b. URL <https://arxiv.org/abs/2410.18912>.
- Tianyuan Zhang, Hong-Xing Yu, Rundi Wu, Brandon Y. Feng, Changxi Zheng, Noah Snively, Jiajun Wu, and William T. Freeman. PhysDreamer: Physics-based interaction with 3D objects via video generation. In *European Conference on Computer Vision (ECCV)*, 2024c. URL <https://arxiv.org/abs/2404.13026>.
- Zhenghao Zhang, Junchao Liao, Menghao Li, Zuozhuo Dai, Bingxue Qiu, Siyu Zhu, Long Qin, and Weizhi Wang. Tora: Trajectory-oriented diffusion transformer for video generation. In *Proceedings of the IEEE/CVF Conference on Computer Vision and Pattern Recognition (CVPR)*, 2025c. URL <https://arxiv.org/abs/2407.21705>.
- Haoyu Zhao, Hao Wang, Xingyue Zhao, Hao Fei, Hongqiu Wang, Chengjiang Long, and Hua Zou. Efficient physics simulation for 3D scenes via MLLM-guided gaussian splatting. In *Proceedings of the IEEE/CVF International Conference on Computer Vision (ICCV)*, 2025. URL <https://arxiv.org/abs/2411.12789>.
- Licheng Zhong, Hong-Xing Yu, Jiajun Wu, and Yunzhu Li. Reconstruction and simulation of elastic objects with spring-mass 3D gaussians. In *European Conference on Computer Vision (ECCV)*, pages 407–423, 2024.

A Appendix

A.1 Online Interactive Playground

We provide an online interactive playground for DeformMaster, where users can select interactive points, adjust material parameters, manipulate the deformable object through keyboard inputs, and inspect synchronized novel-view renderings during rollout. Figure 7 shows the playground interface, including the central interactive view, two novel-view renderers, controller status, material parameter adjustment, and keyboard control panels.

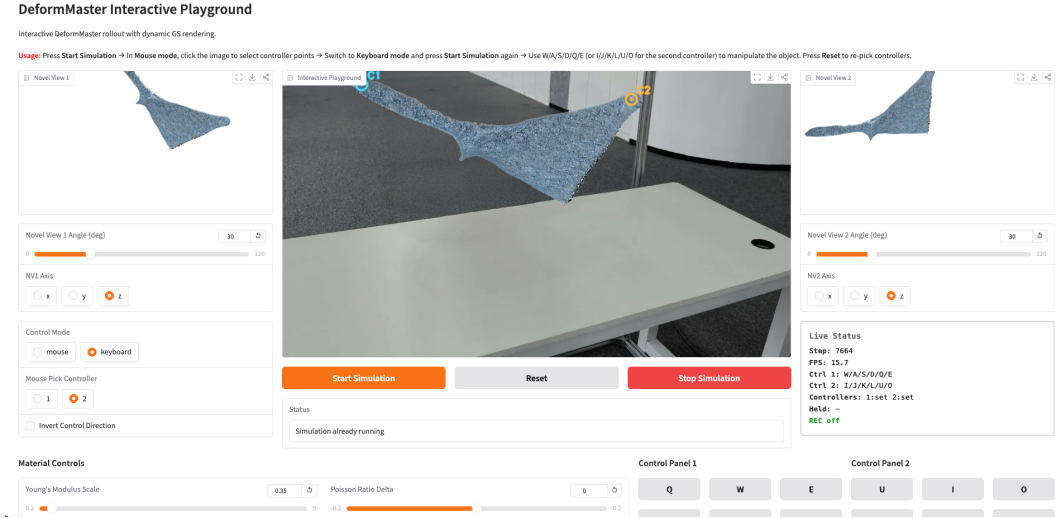


Figure 7: Online interactive playground for DeformMaster. The interface supports interaction-point selection, keyboard-based object manipulation, material-parameter adjustment, and synchronized novel-view rendering during online rollout. The live status panel reports the online rollout speed, showing real-time interaction at over 15 fps in this example.

A.2 Downstream Applications

The interactive world model DeformMaster enables a range of embodied downstream tasks. As shown in Figure 8, its interaction capability can be used to synthesize additional deformable-object data, while the model supports model-predictive-control-based robotic manipulation. The resulting 4D representation also provides convenient visualization and novel-view image synthesis.

A.3 MPM Configuration

Table 3 lists the MPM substrate parameters used throughout training and rollout. Volumetric object interior particle filling follows PhysGaussian [Xie et al., 2024]. One video-frame transition applies $N_{\text{sub}} = \Delta t / \delta t$ MPM substeps. Per-category numeric overrides are noted; values without an override are shared.

A.4 Neural Residual Architecture

The main text describes neural particle-grid residual and gives the encoder equation in Equation (6). Here we provide the decoder and particle-grid interpolation equations that complete the neural residual \mathcal{R}_ϕ .

The encoder E_ϕ is a PointNet [Qi et al., 2017] whose inputs are the post-MPM position $\tilde{\mathbf{x}}_p^{t+1}$ and velocity $\tilde{\mathbf{v}}_p^{t+1}$ of particle p (components of $\tilde{\mathbf{s}}_{t+1}$), the displacement $\tilde{\mathbf{x}}_p^{t+1} - \mathbf{x}_p^t$ accumulated by MPM during the current frame, and the kinematic history h_t of Equation (4). The decoder maps each grid node coordinate \mathbf{x}_g to a node-level correction \mathbf{u}_g using a coordinate-conditioned MLP,

$$\mathbf{u}_g = \alpha \cdot \tanh(D_\phi(\mathbf{f}_p, \gamma(\mathbf{x}_g))), \quad (10)$$

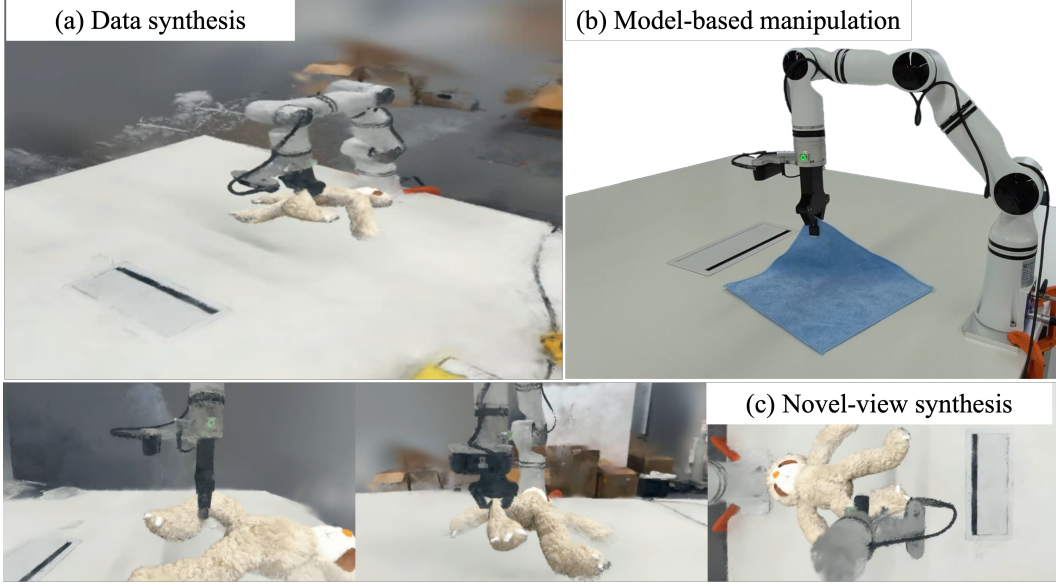


Figure 8: Applications of DeformMaster. (a) DeformMaster leverages interactive manipulation to synthesize additional deformable-object data beyond the observed video. (b) DeformMaster enables model predictive control for deformable-object manipulation. (c) It supports convenient visualization and dynamic novel-view image synthesis.

where D_ϕ is the MLP, $\gamma(\cdot)$ is Fourier positional encoding of the node coordinate, and α is a scalar that bounds the magnitude of the per-particle correction. Finally, the per-particle correction is the B-spline-weighted sum over the surrounding grid nodes,

$$\Delta \mathbf{v}_p = \sum_{g \in \mathcal{N}_p} w_{p,g} \mathbf{u}_g, \quad (11)$$

where \mathcal{N}_p is the set of grid nodes supporting particle p under MPM’s B-spline interpolation, and $w_{p,g}$ are the same interpolation weights used by MPM for P2G/G2P transfers. This mirrors MPM’s particle-grid hybrid at the level of grid discretization and particle-grid transfer: the encoder extracts particle features from the point set, while the decoder predicts local node-wise residuals on each particle’s supporting grid neighborhood before interpolating them back to particles. Concrete network widths and training hyperparameters are listed in Table 4.

A.5 MoCE Parameterization

The main text defines the constitutive mixture at the particle level in Equation (8). The mixture is taken over three canonical hyperelastic experts: **Neo-Hookean (NH)**, **fixed Corotated (Cor)**, and **St. Venant–Kirchhoff (StVK)**, each producing a first Piola–Kirchhoff stress $\mathbf{P}_k(\mathbf{F}_p; E_p, \nu_p)$ from the deformation gradient under shared Young’s modulus and Poisson’s ratio. In the implementation, the learnable physical parameters are stored on a persistent set of material patches and interpolated to particles before each MPM rollout.

Patch centers are sampled once from the first-frame geometry using farthest-point sampling. Each simulation particle p is assigned its three nearest patch anchors $\mathcal{A}(p)$, and the normalized inverse-distance weights

$$\beta_{p,c} = \frac{1/d(\mathbf{x}_p^0, \mathbf{a}_c)}{\sum_{c' \in \mathcal{A}(p)} 1/d(\mathbf{x}_p^0, \mathbf{a}_{c'})}, \quad c \in \mathcal{A}(p), \quad (12)$$

are kept fixed so that patch parameters remain tied to the same material regions during optimization. The expert weights are represented by patch logits $\ell_{k,c}$ and converted to patch probabilities by

$$q_{k,c} = \text{softmax}_k(\ell_{k,c}). \quad (13)$$

Table 3: MPM solver configuration. *linear* / *planar* / *volumetric* columns indicate per-category overrides where they differ from the default.

Group	Symbol / name	Value
<i>Discretisation</i>		
Particles per scene	N	10^5
Background grid	G	32^3
Kernel	cubic B-spline	27-node support
Substep	δt	8×10^{-4} s
Frame interval	Δt	1/30 s
Substeps per frame	$N_{\text{sub}} = \Delta t / \delta t$	42
<i>Forces & boundary</i>		
Gravity	\mathbf{g}	(0, 0, -9.8) m/s ²
Particle damping	—	20.0 (planar/linear), 5.0 (volumetric)
Grid velocity damping	multiplicative per substep	0.999
Position clip	$[\mathbf{x}_{\min}, \mathbf{x}_{\max}]$	$[0.05, 0.95]^3$ (in shifted unit cube)
Floor margin	—	0.0 (planar/linear), 0.05 (volumetric)
<i>Constitutive (per-particle, log-sigmoid bounded)</i>		
Young’s modulus bounds	E	$[10^4, 10^6]$ Pa (planar) $[10^5, 10^7]$ Pa (volumetric)
Poisson ratio bounds	ν	$[0, 0.35]$ (planar) $[0, 0.45]$ (volumetric)
SVD clamp	on \mathbf{F} singular values	$[1/2.0, 2.0]$
Active experts	MoCE (Section A.5)	{NH, Cor., StVK}
<i>Differentiation</i>		
Backend	mpm-pytorch / NVIDIA Warp	differentiable
Truncated-BPTT window	last- W substeps recorded	$W = 20$
Per-parameter clip	on physics gradients	1.0
Global gradient clip	on physics parameters	10.0

The particle-level mixture weights used in Equation (8) are then

$$w_{k,p} = \sum_{c \in \mathcal{A}(p)} \beta_{p,c} q_{k,c}. \quad (14)$$

The same patch-to-particle interpolation is applied to the bounded Young’s modulus and Poisson’s ratio parameters before converting them to Lamé parameters for the MPM stress computation.

A.6 Video Preprocessing Pipeline

Each input clip is processed by a fixed cascade of foundation models that converts raw RGB(-D) frames into the data structures consumed by the trainer (object masks, dense 3D point tracks for the object and the actuator, a first-frame canonical mesh, and calibrated camera intrinsics/extrinsics). The cascade is run once offline per clip and shared across all training stages.

Object segmentation and tracking. Object masks are produced by Grounded-SAM-2 [Ren et al., 2024]: a text prompt naming the target object (e.g. “cloth”, “rope”, “stuffed toy”) is fed to Grounding DINO for open-vocabulary detection on the first frame, the resulting bounding box is passed to SAM 2 to obtain a high-fidelity initial mask, and SAM 2’s video-mode tracker propagates the mask through all T frames. The same pipeline is run with prompt “hand” to obtain a per-frame controller mask, used both to exclude hand pixels from the photometric loss and to anchor actuator positions.

Dense 2D–3D tracking. Within the object mask we sample a dense set of query points on the first frame (farthest-point sampling on the masked region) and propagate them across time with CoTracker3 [Karaev et al., 2024], whose pseudo-label-trained design is robust to occlusion and partial out-of-view. The resulting 2D tracks are unprojected to 3D using the per-frame depth from the next step, producing the dense $(T, N, 3)$ point trajectory that drives the Chamfer/Track losses in $\mathcal{L}_{\text{dynamics}}$.

Table 4: Neural Residual configuration. Values are shared across material categories unless otherwise noted; MPM solver settings (substep, grid, etc.) are listed separately in Table 3.

Group	Symbol / name	Value
<i>Inputs</i>		
Per-particle channels	$9 + 6H$	27 (with $H=3$)
ground fields	pos, vel, frame displacement	9
history	H frames of (pos, vel)	$6H$
Centring	subtract particle-cloud centroid	yes
<i>PointNet encoder (Lagrangian)</i>		
Conv1D widths	$(9+6H) \rightarrow 64 \rightarrow 128 \rightarrow 64$	—
Normalisation	GroupNorm	—
Output	per-particle feature	64-dim
<i>Neural-field decoder (Eulerian)</i>		
Query nodes / particle	MPM B-spline support	27 (cubic kernel)
Decoder grid	co-located with MPM grid	see Table 3
Positional encoding	Fourier bands L	6 (dim 15)
MLP	layers \times width	4×128
Skip connection	every 4 layers	yes
Output activation	$\tanh \cdot \alpha$	$\alpha = 1.0$ m/s
Particle interpolation	B-spline weights (P2G/G2P)	27-node
Residual cadence	once per frame (post all substeps)	—
<i>Optimisation</i>		
Optimiser	Adam	$\beta_1=0.9, \beta_2=0.999$
Learning rate	η_ϕ	5×10^{-3}
Gradient norm clip	—	5.0
Residual regulariser	$\lambda_{\text{reg}} \ \Delta \mathbf{v}\ ^2$	$\lambda_{\text{reg}} = 10^{-3}$
Differentiability	MPM via Warp autodiff	end-to-end
Truncated-BPTT window	MPM tape length (in substeps)	see Table 3

Monocular geometry (uncalibrated single-camera setting). For monocular sequences we estimate per-frame depth and camera pose with Depth Anything 3 [Lin et al., 2026], which jointly outputs depth maps and any-view pose. We resolve global scale by fitting a per-clip scale factor that aligns its predictions with the metric point map produced by MoGe-2 [Wang et al., 2025] on the masked object; we minimize the median absolute residual to suppress outliers, and apply the recovered affine to all DA3 depth maps. This DA3+MoGe-2 fusion preserves DA3’s pose accuracy while absorbing MoGe-2’s metric-scale geometric prior.

Shape generative prior. To initialize particles in regions occluded at $t=0$, we use TRELIS [Xiang et al., 2025] to generate a canonical textured mesh from the segmented first frame. The mesh is aligned to the observed first-frame point cloud by rendering candidate mesh views, selecting the best match to the real RGB crop with SuperGlue [Sarlin et al., 2020] keypoint matching, solving the 6-DoF pose with PnP, and then refining it with an ARAP regularizer. The aligned mesh is volumetrically sampled together to populate the MPM particles.

A.7 Training Details

Compute. All training and inference are conducted on a single NVIDIA A100 GPU. Per scene, Stage 1+2 dynamics training takes approximately 2–3 hours of wallclock time, and Stage 3 appearance learning and RGB-guided refinement adds a comparable amount; peak GPU memory stays within ~ 20 GB, well within the 80 GB capacity of one A100.

Stage 1–2 alternating optimization. The interactive physics–neural dynamics is implemented with a mixed NVIDIA Warp/PyTorch backend: the MPM simulator runs in Warp, while the neural residual is implemented in PyTorch. The MPM step is differentiable end-to-end via NVIDIA Warp’s autodiff backend, so the residual is optimised jointly with the physics parameters rather than in two stages.

Stages 1 and 2 are coupled: DCA gains (k_p, k_d) and material fields are mutually dependent through the simulator rollout. We therefore alternate between gradient-based dynamics training and gradient-

free gain selection. We first optimize the material fields and neural residual with default gains, then run CMA-ES gain selection using the warm-started dynamics, and finally continue optimizing the material fields and neural residual with the selected gains.

We add a small ℓ_2 penalty $\lambda_{\text{reg}} \|\Delta \mathbf{v}\|^2$ to the training loss to discourage unnecessary correction; the value of λ_{reg} is given in Table 4, and the truncated-BPTT horizon over which gradients are propagated is set by the MPM tape window in Table 3.

RGB-guided refinement in Training Stage 3. Stage 3 has two steps. We first optimize a first-frame Gaussian Splatting representation \mathcal{G}_0 with appearance supervision, then freeze \mathcal{G}_0 and resume from the Stage 2 dynamics checkpoint for 30 additional iterations. During this refinement step, \mathcal{G}_0 is deformed by linear blend skinning along the predicted particle trajectory $\mathbf{x}_{1:t}$, rasterised through each training-view camera, and compared to the recorded frame using a masked ℓ_1 RGB loss. Object pixels retain their captured RGB, background pixels are set to the renderer background to penalize Gaussian bleed, and hand pixels are excluded because the renderer contains no hand model. The refinement loss keeps the dynamics terms and adds RGB supervision, $\mathcal{L}_{\text{stage3}} = \mathcal{L}_{\text{dynamics}} + \lambda_{\text{rgb}} \mathcal{L}_{\text{rgb}}$ with $\lambda_{\text{rgb}} = 10^{-2}$. Because \mathcal{G}_0 is deformed from the predicted particle trajectory, the photometric gradient flows through LBS back to particle motion and the neural residual, acting as an RGB-guided constraint on the dynamics rather than an update to the frozen Gaussians.

A.8 Limitations

DeformMaster still has several limitations. First, particle-grid simulation is less specialized for very thin planar objects, such as single-layer cloth, than spring-mass systems with fixed topological links. This is reflected by the remaining gap to PhysTwin on planar object Track (Section 4.2), where explicit spring-mass connectivity provides a strong inductive bias for cloth-like bending and stretching. Second, interaction modeling relies on observed hand motion. When the hand or actuator is severely occluded in the input video, the recovered interaction signal can be incomplete, which in turn degrades the action-conditioned rollout. Third, runtime depends on the number of physics substeps used during simulation. Reducing the substep count of the MPM solver improves real-time performance, whereas high-accuracy deformation simulation often requires more substeps; this creates a trade-off between fidelity and runtime.

A.9 Ablation Details

Tables 5 to 12 provide the full numerical ablations for the residual branch, DCA, MoCE, and Stage 3 RGB-guided dynamics refinement. Each ablation is reported in two views: an *overall* table with all six paper metrics (Tables 5, 7, 9 and 11) and a *per-category* dynamics table grouped by Linear / Planar / Volumetric (Tables 6, 8, 10 and 12).

Table 5: Residual ablation: overall test metrics on the 20-case PhysTwin benchmark. Chamfer and Track in units of 10^{-2} .

Variant	Future dynamics			Future appearance		
	IoU \uparrow	Chamfer \downarrow	Track \downarrow	PSNR \uparrow	SSIM \uparrow	LPIPS \downarrow
Ours (PNPGD)	0.748	1.14	2.40	25.41	0.936	0.061
MLP	0.735	1.27	2.59	25.16	0.935	0.063
GNN	0.715	1.44	2.78	24.68	0.932	0.068
No residual	0.656	2.12	3.94	23.90	0.929	0.076

Table 6: Ablation on the residual branch \mathcal{R}_ϕ : per-category dynamics on the PhysTwin benchmark. Chamfer and Track in units of 10^{-2} . **Ours**: neural particle-grid. **MLP**: per-particle correction with no spatial structure. **GNN**: 3-round KNN graph network. **No residual**: pure MPM rollout.

Variant	Linear ($n=3$)			Planar ($n=9$)			Volumetric ($n=8$)		
	IoU \uparrow	Chamfer \downarrow	Track \downarrow	IoU \uparrow	Chamfer \downarrow	Track \downarrow	IoU \uparrow	Chamfer \downarrow	Track \downarrow
Ours	0.721	0.50	1.01	0.748	1.30	3.19	0.756	1.19	2.02
MLP	0.727	0.52	1.04	0.733	1.45	3.43	0.739	1.35	2.21
GNN	0.700	0.57	1.19	0.719	1.66	3.63	0.714	1.52	2.42
No residual	0.628	0.78	1.48	0.695	2.08	4.52	0.614	2.67	4.20

Table 7: DCA ablation: overall test metrics. Chamfer and Track in units of 10^{-2} . \ddagger rigid is averaged over the 11/20 sequences that survived training (the 8 Volumetric and 1 Linear that diverged are excluded).

Variant	Future dynamics			Future appearance		
	IoU \uparrow	Chamfer \downarrow	Track \downarrow	PSNR \uparrow	SSIM \uparrow	LPIPS \downarrow
DCA (ours)	0.748	1.14	2.40	25.41	0.936	0.061
rigid \ddagger	0.713	1.44	3.25	24.51	0.927	0.078
single actuator	0.561	3.08	6.19	22.32	0.914	0.102

Table 8: DCA ablation: per-category dynamics. Chamfer and Track in units of 10^{-2} . **rigid** (no compliance): replace compliant coupling with hard Dirichlet boundary. **single actuator** (no distribution): keep compliance but actuate each particle through a single actuator instead of a distributed contact patch. “NaN” marks the 8 Volumetric sequences that diverged near iteration 0 under hard pointwise constraints; \dagger rigid completes only 2/3 Linear sequences.

Variant	Linear ($n=3$)			Planar ($n=9$)			Volumetric ($n=8$)		
	IoU \uparrow	Chamfer \downarrow	Track \downarrow	IoU \uparrow	Chamfer \downarrow	Track \downarrow	IoU \uparrow	Chamfer \downarrow	Track \downarrow
DCA (ours)	0.721	0.50	1.01	0.748	1.30	3.19	0.756	1.19	2.02
rigid	0.675 \dagger	0.51 \dagger	1.14 \dagger	0.718	1.65	3.72	NaN	NaN	NaN
single actuator	0.510	0.92	2.40	0.591	2.74	5.69	0.534	4.26	8.16

Table 9: MoCE ablation: overall test metrics. Chamfer and Track in units of 10^{-2} .

Variant	Future dynamics			Future appearance		
	IoU \uparrow	Chamfer \downarrow	Track \downarrow	PSNR \uparrow	SSIM \uparrow	LPIPS \downarrow
MoCE (ours)	0.748	1.14	2.40	25.41	0.936	0.061
Single Neo-Hookean	0.658	1.94	3.75	23.84	0.928	0.077

Table 10: Constitutive ablation: replacing the MoCE mixture with a single canonical Neo-Hookean expert. Per-category dynamics on the PhysTwin benchmark; Chamfer and Track in units of 10^{-2} . (The MoCE ablation keeps the neural residual active. Since the residual can absorb part of the mismatch caused by a simplified constitutive model, this comparison may underestimate the contribution of MoCE.)

Variant	Linear ($n=3$)			Planar ($n=9$)			Volumetric ($n=8$)		
	IoU \uparrow	Chamfer \downarrow	Track \downarrow	IoU \uparrow	Chamfer \downarrow	Track \downarrow	IoU \uparrow	Chamfer \downarrow	Track \downarrow
MoCE (ours)	0.721	0.50	1.01	0.748	1.30	3.19	0.756	1.19	2.02
Single Neo-Hookean	0.642	0.69	1.48	0.693	2.04	4.65	0.617	2.30	3.59

Table 11: Stage 3 RGB-guided refinement: overall test metrics. Chamfer and Track in units of 10^{-2} .

Variant	Future dynamics			Future appearance		
	IoU \uparrow	Chamfer \downarrow	Track \downarrow	PSNR \uparrow	SSIM \uparrow	LPIPS \downarrow
Dynamics loss only	0.745	1.16	2.43	25.32	0.935	0.062
RGB-guided refinement (ours)	0.748	1.14	2.40	25.41	0.936	0.061

Table 12: Ablation of RGB-guided dynamics refinement in Stage 3. Per-category dynamics on the PhysTwin benchmark; Chamfer and Track in units of 10^{-2} .

Variant	Linear ($n=3$)			Planar ($n=9$)			Volumetric ($n=8$)		
	IoU \uparrow	Chamfer \downarrow	Track \downarrow	IoU \uparrow	Chamfer \downarrow	Track \downarrow	IoU \uparrow	Chamfer \downarrow	Track \downarrow
Dynamics loss only	0.725	0.50	1.01	0.743	1.33	3.22	0.752	1.22	2.08
RGB-guided refine	0.721	0.50	1.01	0.748	1.30	3.19	0.756	1.19	2.02